Available online at www.sciencedirect.com
ScienceDirect
International Journal of Heat and Mass Transfer 49 (2006) 4712–4720
International Journal of HEAT and MASS TRANSFER
www.elsevier.com/locate/ijhmt

In situ investigation of water transport in an operating PEM fuel cell using neutron radiography: Part 1 – Experimental method and serpentine flow field results

T.A. Trabold [a], J.P. Owejan [a,*], D.L. Jacobson [b], M. Arif [b], P.R. Huffman [c]

[a] General Motors Fuel Cell Activities, 10 Carriage Street, Honeoye Falls, NY 14472, USA
[b] National Institute of Standards and Technology (NIST), Center for Neutron Research, 100 Bureau Drive, Gaithersburg, MD 20899, USA
[c] Department of Physics, North Carolina State University, Raleigh, NC 27695, USA

Received 18 May 2005; received in revised form 30 June 2006
Available online 20 September 2006

Abstract

Effective management of liquid water produced in the cathodic reaction of a polymer electrolyte membrane (PEM) fuel cell is essential to achieve high cell efficiency. Few experimental methods are available for in situ measurements of water transport within an operating cell. Neutron radiography is a useful tool to visualize water within a cell constructed of many common materials, including metals. The application of neutron radiography to measurements of water content within the flow field channels of an operating 50 cm^2 PEM fuel cell is described. Details of the experimental apparatus, image processing procedure and quantitative analysis are provided. It is demonstrated that water tends to accumulate in the 180° bends of the serpentine anode and cathode flow fields used in this study. Moreover, the effects of both the current density and cathode stoichiometric ratio on the quantity of accumulated water are discussed.

Keywords: Fuel cell; PEM; Neutron radiography; Water management; Two-phase flow

1. Introduction

Fuel cells have recently become the subject of significant research and development activity, as they offer the possibility of low emissions, high efficiency power for portable, stationary, and vehicular applications. Proton exchange membrane (PEM) fuel cells combine hydrogen and oxygen (usually from air) to produce electrical current with only water and heat as by-products. As illustrated in Fig. 1, the heart of the device is the membrane electrode assembly (MEA), which consists of a polymer membrane coated on both sides with a catalytic electrode layer. The anode and cathode electrodes are typically comprised of platinum supported on carbon black particles in a proton-conducting ionomer binder. On either side of the MEA are anode and cathode backing layers, more commonly referred to as gas diffusion layers (GDL). These components are porous carbon-based materials, usually either fibrous paper or woven cloth, that distribute reactant gas flows from the flow field channels to the electrode layers on the MEA. Both the GDL and flow field plates also satisfy the role of conducting electrons and heat through the fuel cell. Therefore, these components are constructed of materials with relatively high electrical and thermal conductivity. Humidified reactant gases diffuse from the channels through the porous GDL to the catalytic reaction sites on the platinum electrodes. Most of the water that is produced on the cathode side of the MEA via the oxygen reduction reaction is transported back through the GDL into the cathode flow field channels and then is eventually removed from the fuel cell by the gas flow and gravity if so oriented. To achieve a required power load, multiple fuel

* Corresponding author. Tel.: +1 585 624 6802; fax: +1 585 624 6680.
E-mail address: jon.owejan@gm.com (J.P. Owejan).

0017-9310/$ - see front matter © 2006 Elsevier Ltd. All rights reserved.
doi:10.1016/j.ijheatmasstransfer.2006.07.003

Nomenclature

d	diameter of circular aperture in neutron beam system (cm)	N	atomic density (cm^{-3})
I	transmitted neutron beam intensity	T	material thickness (cm)
I_0	incident neutron beam intensity	*Greek symbol*	
L	distance of test section from circular aperture (m)	σ	material neutron cross-section (cm^2)

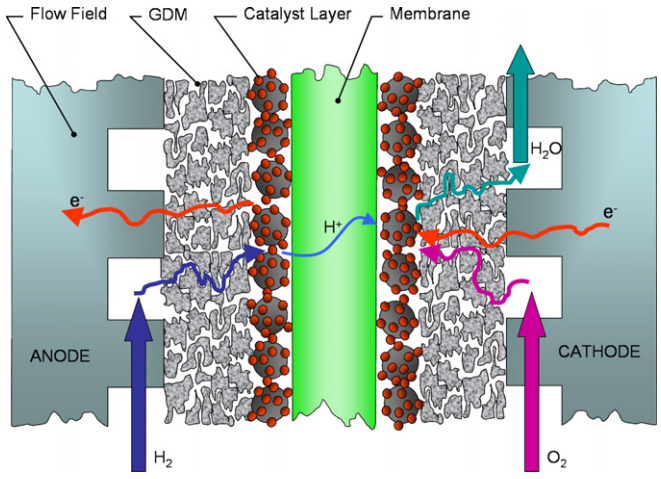

Fig. 1. Key components of a PEM fuel cell (not to scale). Descriptions of individual components are given in the text.

cells can be stacked in a series arrangement so that additional cells add voltage output at the same current. In this sense, fuel cells are easily scalable from very small loads requiring one or two cells, up to automotive and high-end stationary units which can have hundreds of cells connected in series.

The polymer membrane affords conduction of protons (H^+ ions) that are produced by hydrogen oxidation on the anode side of the fuel cell. The membrane is impervious to electrons which must instead flow around the membrane through an external load. It is this flow of electrons that provides the fuel cell power. After passing through the load, the electrons then re-combine with the H^+ ions and oxygen from air introduced on the cathode side to form water as the main reaction product. The proper management of the water produced in the cathodic oxygen reduction reaction is essential to achieve efficient operation. While the polymer membrane and catalyst ionomer must be well hydrated to facilitate proton transfer, if excess water is present, reactant oxygen will be restricted from reaching catalytic sites at the electrode surface. This phenomenon, often referred to in general terms as "flooding", essentially increases the resistance to reactant flow within the fuel cell.

There is much activity within the fuel cell community to develop measurement methods that will aid in assessing all aspects of fuel cell operation. Measurements of local current density, membrane resistance, oxygen concentration, and gas humidification within operating cells have been reported (e.g., [1,2]). However, ascertaining where liquid water is accumulated within the fuel cell, and how it is transported on both the anode and cathode sides, remains a difficult experimental problem. Recently, novel experimental designs have been reported that enable visualization of two-phase flow in the cathode flow field channels of a PEM fuel cell. For example, Tuber et al. [3] and others have used fuel cells with windows in the backing plates to afford visual access. However, this approach limits visualization to the process of water droplets passing from the diffusion medium into the flow field channels. Moreover, it is difficult to modify the fuel cell hardware in this manner without affecting the thermal behavior during operation. Perhaps the only method available for measuring full-area water distribution within an operating fuel cell, including that present within the porous materials described below, is the neutron radiography technique. Because of the high neutron attenuation of hydrogeneous materials relative to other common materials used in fuel cell construction, this technique is ideally suited to interrogate an operating fuel cell for liquid water. Several research organizations, including the National Institute of Standards and Technology (NIST) and the Pennsylvania State University in the US, and Paul Scherrer Institut (PSI) in Switzerland, have developed a high level of expertise in this field. These organizations have reported experimental work on the application of neutron radiography to fuel cells [4–8].

The present paper describes an investigation of the application of neutron radiography as a diagnostic tool for evaluating water transport in a 50 cm^2 fuel cell. Details of the experimental apparatus, image acquisition and processing procedures are provided. The initial experimental results demonstrate the ability of the method to clearly isolate the two-dimensional location and quantity of accumulated liquid water. Moreover, the effects of fuel cell operational parameters, such as the current density and cathode stoichiometric ratio, on how water is retained can be isolated and quantified.

2. Experimental apparatus and test procedure

The experimental apparatus consists of three separate systems: a neutron source, an operating PEM fuel cell with active area of 50 cm^2, and a scintillator/CCD imaging

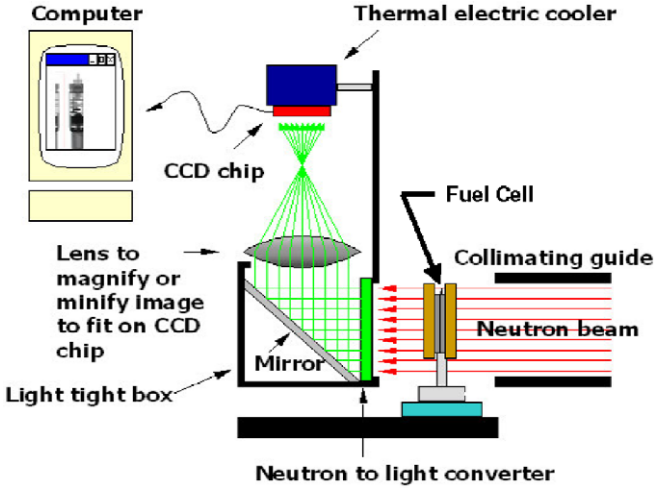

Fig. 2. Schematic illustration of the neutron radiography apparatus.

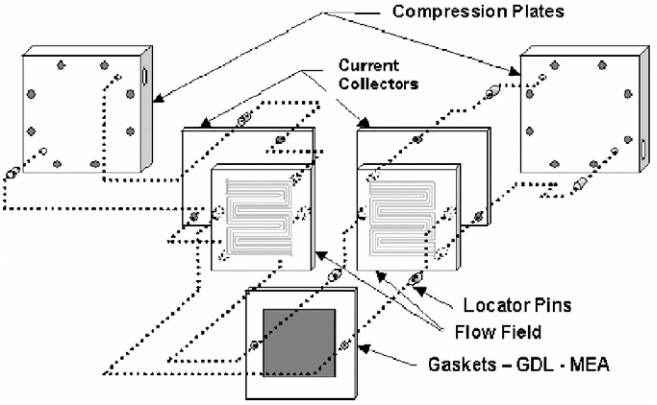

Fig. 3. Exploded view of the 50 cm^2 fuel cell used in these measurements.

station. The fuel cell test section is mounted normal to a collimated neutron beam with a scintillator screen directly behind to convert transmitted neutrons to photons, which are captured with a charge coupled device (CCD) array (Fig. 2).

2.1. 50 cm^2 fuel cell design and operation

The 50 cm^2 PEM fuel cell is constructed with 2.54 cm thick aluminum compression plates on the outermost ends of the assembly (Fig. 3). Gold-coated copper current collector plates of 0.16 cm thickness are insulated from the adjacent compression plates. The anode and cathode flow field channels are machined into 10.2 cm square, 1.3 cm thick graphite blocks. Between the anode and cathode flow fields, the membrane-electrode assembly (MEA) and gas diffusion layers (GDL) are compressed, using gaskets with the appropriate thickness to provide 20% compressive strain of the two GDL layers. For all experiments conducted in this study, the MEAs were comprised of 25 μm thick Gore 5510 membranes (W.L. Gore & Associates),[1] and 0.4 mg platinum per square centimeter in both of the anode and cathode electrode layers. The GDL were carbon fiber papers manufactured by Toray with thickness of about 180 μm, and treated with 7% by mass polytetrafluoroethylene (PTFE).

The anode and cathode flow field channels each form a serpentine pattern across the active area of the 50 cm^2 fuel cell. The anode flow field utilizes a 2-channel, 23 pass serpentine pattern with a channel width and depth of 0.84 mm and 1.12 mm, respectively, and a land width of 0.71 mm. The cathode flow field is designed to maintain approximately the same overall pressure differential as the anode, thereby minimizing pressure gradients across the MEA. This design requires a 3-channel, 15 pass serpentine pattern with a channel width and depth of 0.89 and 0.84 mm, respectively, and a land width of 0.66 mm.

The Teledyne Energy Systems MEDUSA™ PEM fuel cell test station model 890C was employed for all fuel cell operation and control requirements. The system is utilized for gas humidification, gas pressure and flow control, cell temperature control, load control, and for data logging. The heated inlet lines are controlled with separate PID controllers to 5 °C above the dew point of the reactant gas to minimize inlet condensation. The mass flow controllers and humidifiers are calibrated to ensure proper test stand operation in the range of interest for the present study.

2.2. Neutron radiograph acquisition and image processing

The neutron radiography experiments were conducted at the National Institute of Standards and Technology (NIST) Center for Neutron Research (NCNR) with a thermal neutron research reactor fueled by ^{235}U. The reactor is a split core design, leaving a D_2O water gap capable of being viewed through 8 beam tubes and a liquid H_2 cold source. Viewing the gap instead of directly viewing the fuel sections allows for a dramatic reduction in high energy neutrons and gamma rays that contribute to background levels.

These experiments were conducted using neutrons from the thermal neutron beam tube BT-6. This facility provides a highly collimated intense source of thermal neutrons incident normal to the test section. This optical design places a neutron absorbing circular aperture between the reactor core and the test section viewing the reactor core as if through a pinhole camera. If the distribution of neutron intensity at the core is uniform then the distribution of neutron intensity at the test section will also be uniform. It is important to have a uniform neutron fluence rate at the test position. By adjusting the diameter (d) of the circular aperture and the distance between the test section and the aperture (L), the geometric sharpness of the neutron shadow of

[1] Certain trade names and company products are mentioned in the text or identified in illustrations in order to adequately specify the experimental procedure and equipment used. In no case does such identification imply recommendation or endorsement by the National Institute of Standards and Technology, nor does it imply that the products are necessarily the best available for the purpose.

the test section can be controlled. The geometric sharpness is directly proportional to the ratio of L/d. This is extremely important since the neutron image of the shadow is formed downstream from the test section. The farther the neutron imaging system is away from the test section, the more the edges in the image will be blurred. If the L/d ratio is too low then the resolution of the image may be substantially lower than the neutron imaging system. Generally, values of L/d of 300 or more are considered adequate for the resolution scales that a typical neutron imaging system is capable of achieving.

For this experiment, $d = 1$ cm and $L = 4$ m, providing an L/d ratio of 400. At the detector position directly behind the test section, the neutron beam intensity is 2×10^7 cm^{-2} s^{-1} and is uniformly distributed (to within 20%) over an area 15 cm in diameter. The neutron beam is first filtered of high energy neutrons and gamma rays using a 10 cm thick, liquid nitrogen cooled, bismuth single crystal filter before passing through the pinhole that defines d. Bismuth preferentially transmits thermal neutrons relative to high energy neutrons and gammas. Filtering out these components of the beam allows significant reduction of the amount of shielding needed near the test section.

The neutron beam passes through the fuel cell located a distance L from the pinhole aperture. About 10 cm downstream from the fuel cell, the two-dimensional image of the neutron beam is recorded using a CCD camera. The neutrons are first captured in a thin neutron scintillator screen that is 20 cm by 20 cm by 0.03 cm thick. The scinitillator is a matrix of ZnS with Cu and ^{6}Li. The neutrons are absorbed by the ^{6}Li with total efficiency of about 20%. The reaction by-products deposit energy into the ZnS matrix, which produces visible light as the atoms de-excite. The Cu ensures that the distribution of the light yield is preferentially weighted around the wavelength 550 nm, to maximize the efficiency of light collection in the CCD camera.

The spatial resolution is limited by blooming of the scintillation light. Typically the light blooms to several hundred microns in diameter resulting in sharp edges being blurred. The resulting spatial resolution can be quantified by measuring the blurring of a neutron shadow cast by a sharp absorbing edge. This edge is formed using a 25 μm thick, neutron absorbing foil of gadolinium; Gd has a large cross-section for thermal neutron capture ($\sigma_a = 3 \times 10^4$ barns). From the Fourier transform of the edge spread function, one obtains the modulation transfer function (MTF). The spatial frequency where this function falls to 10% of the maximum MTF is the standard measure of spatial resolution. For our geometry, this value is two line pairs per mm, which represents a spatial frequency of 250 μm.

The light images from the scintillator screen are digitized as a two-dimensional matrix of count or gray level values using a CCD camera. The CCD camera was an Apogee AP6 camera that converts analog to digital with a 14 bit depth. The CCD pixel matrix is 1024 × 1024 with the gray level values stored as 16 bit integer values. The CCD was focused on a 14 cm diameter area allowing a 10 cm × 10 cm area to be digitized. Each pixel then corresponds to a 100 μm × 100 μm area on the scintillator screen. The images are then stored using the FITS (Flexible Image Transport System) format and processed using IDL (Interactive Data Language) software from Research Systems Inc. The FITS format allows the images to be converted to and stored as floating point images which is advantageous for image processing.

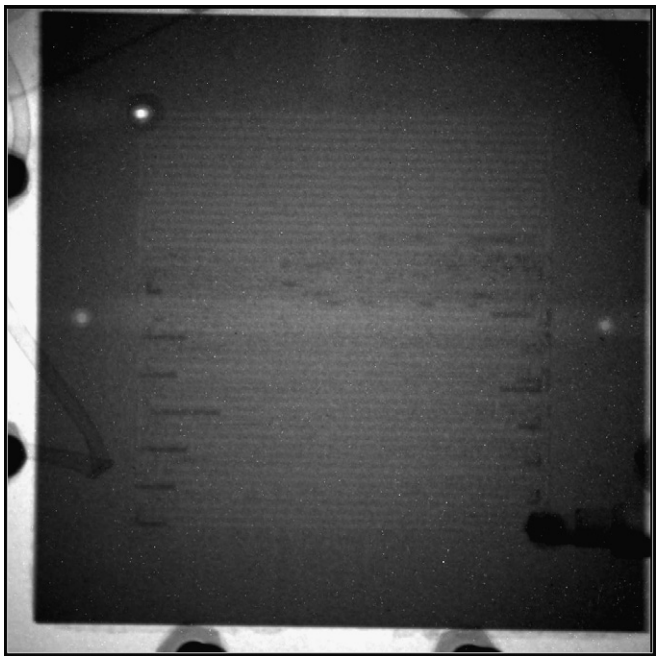

Fig. 4. Radiograph of an operating fuel cell. The dark areas correspond to larger neutron absorption (or scattering) than the lighter areas.

For the raw images, histograms of the number of counts vs. pixel value range show that most of the pixels had between 600 counts and 1500 counts, where 1 count equals 1 neutron event at the scintillator. Because the maximum count scale available was 2^{14} or 16,384, the dynamic range of the CCD sensor was not being fully utilized. A typical image acquired during cell operation is shown in Fig. 4, where the intensity levels represent the magnitude of counts in the CCD camera from black (600 counts, maximum relative absorption) to white (1500 counts, minimum absorption). Two features of this image worth noting are the faint light region in the center of the cell corresponding to horizontal holes bored into the backing plates,[2] and the reactant gas exhaust fitting in the lower right-hand corner that has water present in its lower half.

The neutron beam intensity of the wet (i.e., operating) fuel cell image is normalized to the image of the dry (i.e.,

[2] This hole accommodates heater rods that were not used in the present study. Alternatively, ribbon heaters were attached to the outside edge of the fuel cell assembly to control temperature without interfering with the neutron beam path.

non-operating) fuel cell. Before this normalization takes place, the background image is subtracted. This background image, acquired with the neutron beam turned off and with the CCD camera shutter open, contains the following additive biases that are present in all images acquired:

- Read noise – associated with how the digitizer reads out the CCD and can be subtracted from the image; usually several counts.
- Dark current – noise per pixel that is due to thermal noise in the CCD. Cooling the CCD minimizes this dark current noise; however, it will always be present and will vary with the time of the exposure.
- Spurious light – minute amounts of ambient light that enter through the CCD enclosure.

To isolate the water formation in the fuel cell, the wet images were normalized using a dry fuel cell image instead of the unattenuated beam image, with a typical radiograph shown in Fig. 5. Artifacts due to inhomogeneity in the beam intensity or imaging system, or extraneous features of the fuel cell hardware, are minimized by this normalization procedure.

Once the normalized water image is obtained, one can compute the local water thickness at each pixel location. The neutron attenuation through a material is given by

$$I = I_0 \, \mathrm{e}^{-N\sigma T} \tag{1}$$

where I and I_0 are the transmitted and incident neutron beam intensities, respectively $(\mathrm{cm}^2\,\mathrm{s})^{-1}$, N is the atomic density (atoms/cm^3), σ is the neutron cross-section (cm^2) and T is the thickness of the beam attenuating medium (cm). If the attenuating medium contains more than one material, then Eq. (1) may be generalized by

$$I = I_0 \, \mathrm{e}^{-\sum_i (N\sigma T)_i} \tag{2}$$

Under conditions when the fuel cell is dry (i.e., non-operating), Eq. (2) describes the transmission through all the components that do not change over the course of the subsequent experiments, including the backing plates, current collectors, flow field plates, dry membrane and dry diffusion media materials. Thus, in an operating cell, the only attenuating materials that are not accounted for in the dry image are liquid water, water vapor, hydrogen, oxygen, and nitrogen. For an operating cell, Eq. (2) can therefore be written as

$$I = I_0 \, \mathrm{e}^{-\left[\sum_i (N\sigma T)_{i,\mathrm{dry}} + (N\sigma T)_{\mathrm{w,l}} + (N\sigma T)_{\mathrm{w,v}} + (N\sigma T)_{\mathrm{H_2}} + (N\sigma T)_{\mathrm{O_2}} + (N\sigma T)_{\mathrm{N_2}}\right]} \tag{3}$$

By dividing Eq. (3) by the dry cell image, and further considering that the product $N\sigma$ for liquid water is much greater that for any of the gaseous components, we have

$$\frac{I_{\mathrm{wet}}}{I_{\mathrm{dry}}} = \mathrm{e}^{-(N\sigma T)_{\mathrm{w,l}}} \tag{4}$$

From Eq. (4), the final expression for the product $N\sigma T$ for liquid water is

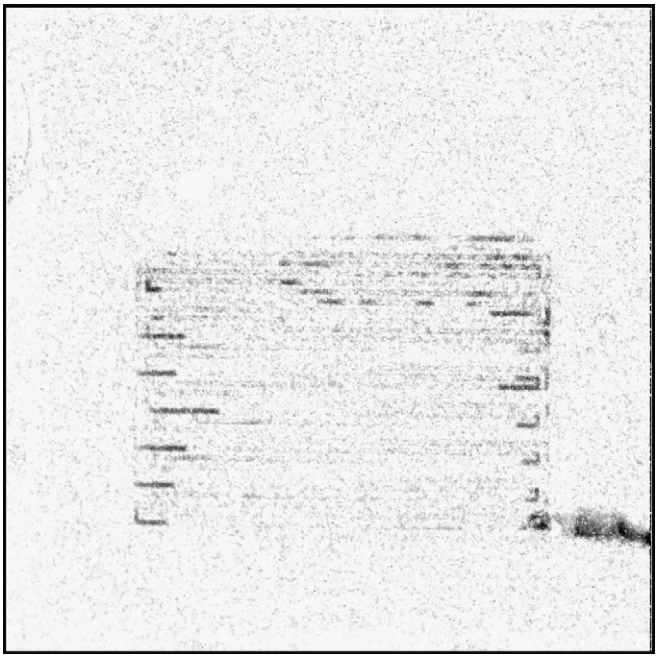

Fig. 5. Radiograph obtained by normalizing the operating cell image (Fig. 4) by a dry cell image as described in the text. The dark areas correspond to areas within the fuel cell that contain water.

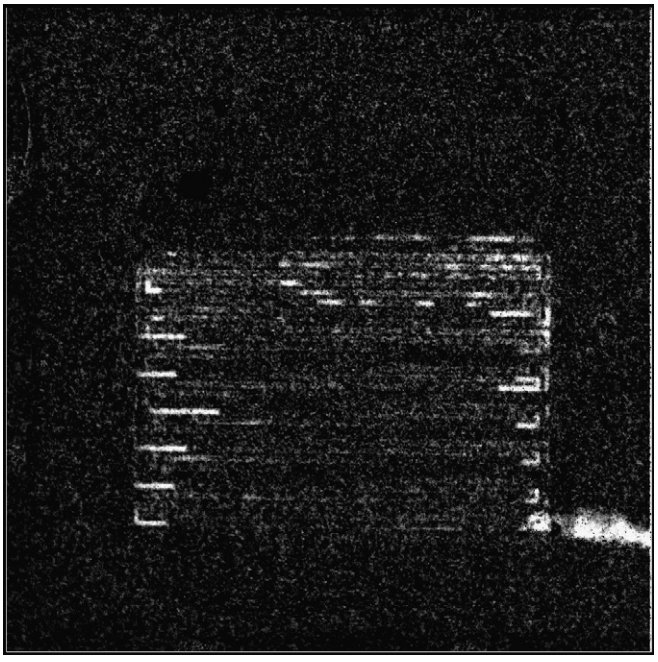

Fig. 6. The natural logarithm of each pixel in Fig. 5, corresponding to the product of the neutron cross-section, atomic density, and water thickness ($N\sigma T$).

$$N\sigma T = -\ln\left(\frac{I_{wet}}{I_{dry}}\right) \quad (5)$$

Fig. 5 shows a normalized transmission image of an operating fuel cell as described by Eq. (4). The product $N\sigma T$ is then obtained by computing the negative natural logarithm of each pixel fraction less than one in Fig. 5, as illustrated in Fig. 6. Less than 1% of pixel values are slightly greater than one as a result of noise, but are eliminated through the image averaging process described below.

Although the images in Figs. 4–6 clearly show variations in liquid water content associated with variations in gray scale, it is difficult to visualize small gradients because the maximum dynamic range of values present in the gray scale images is set at 256 levels. Color scales exaggerate image gradients to allow one to view a larger dynamic range of information. To create a color image from a gray scale image, the gray scale array of $N\sigma T$ values from 0 to 0.15 in Fig. 6 was mapped to an RGB scale, as shown in Fig. 7. The resulting image emphasizes the gradients in liquid water thickness, and features such as the accumulation of water in the 180° bends of the flow field channels. Fig. 7, however, still shows a significant level of noise because of the limited statistics in a single CCD image with a shutter time of 1 s. By averaging n consecutive images, the random noise component is reduced by the factor $n^{-1/2}$. In Fig. 8, 120 images have been averaged and then colorized in the same manner as previously described. This averaging produces an image with a higher signal-to-noise ratio that provides detailed information on the location and relative quantities of accumulated water. Because the image acquisition rate was one image per 3.8 s (1 s exposure, 2.8 s file write), the final average image was acquired over a period of 7.6 min.

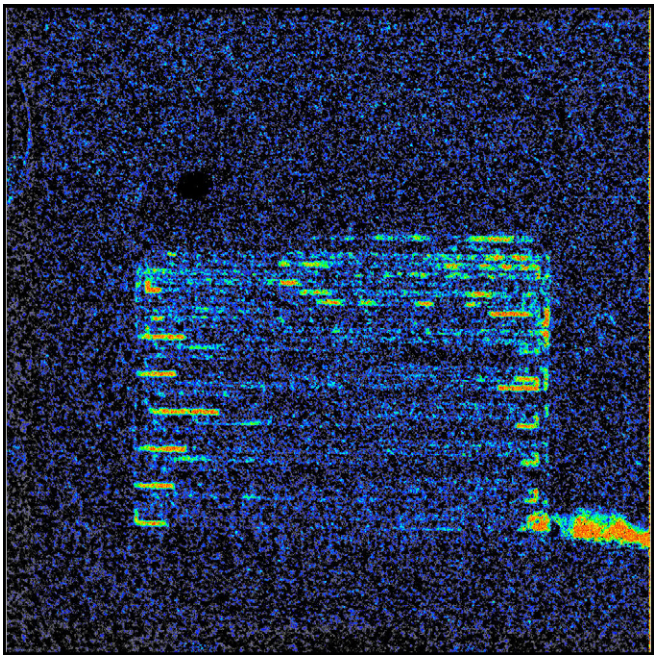

Fig. 7. Color image of $N\sigma T$ obtained by mapping the gray scale in Fig. 6 to RGB scale as described in the text.

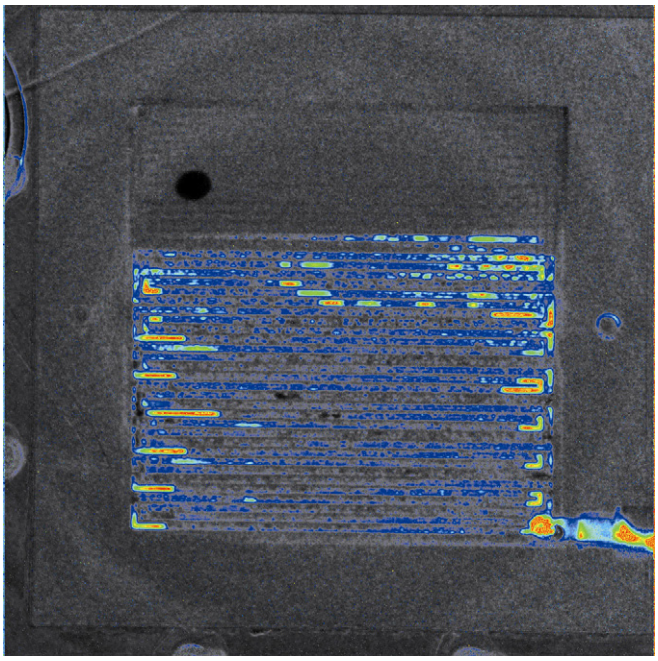

Fig. 8. Time-averaged color image of $N\sigma T$ consisting of 120 consecutive images occurring over a time period of 7.6 min.

3. Results and discussion

The image acquisition and processing procedure described above was used to investigate water transport and accumulation over various operational conditions for the 50 cm^2 fuel cell described in Section 2. This initial study was used to investigate how water accumulation in the channels of the anode and cathode flow field plates changes the fuel cell operational performance in the range of current densities from 0.1 A/cm^2 to 1.0 A/cm^2. Therefore, it was useful to isolate the water behavior in the channels while disregarding image features outside of the active area of the cell, such as the significant accumulation in the exhaust gas fitting. Image "masks" were developed from the engineering drawings for the anode and cathode flow fields. These masks were matrices wherein pixels falling within the domain of either of the flow field channels were assigned a value of 1, while pixels outside the channels were assigned a value of 0. Fig. 9 shows the time averaged fuel cell image before (left) and after (right) the image masking operation was applied. Note that the RGB color scale has been expanded to represent a range of $N\sigma T$ values from 0 to 0.05, instead of 0–0.15 as in Figs. 7 and 8. This change was made to depict water distributions over a wider range of operating conditions, including some where relatively little water was present.

In Fig. 10, time-averaged water distribution images are shown for current densities of 0.1 A/cm^2, 0.5 A/cm^2, and 1.0 A/cm^2, and under the following conditions: 80 °C,

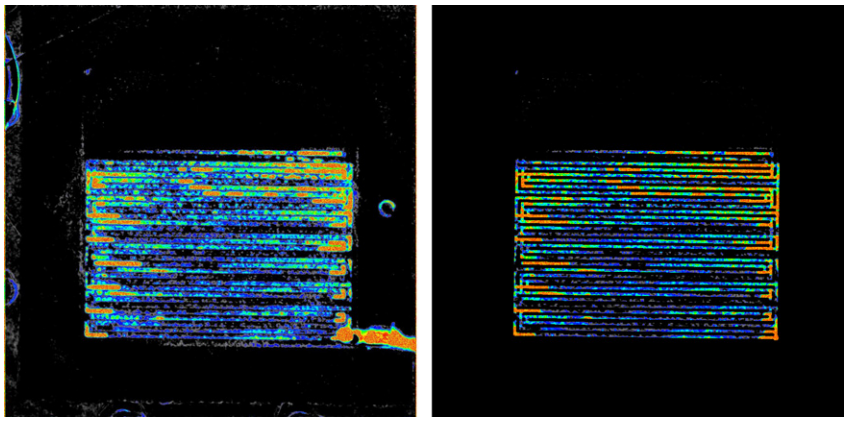

Fig. 9. Anode and cathode channel masking operation. The image on the left is masked to isolate the flow channels, producing the image on the right. Details of the masking procedure are described in the text.

270 kPa back pressure, fully humidified reactant flows and anode and cathode stoichiometric ratios of 2 and 1.3, respectively. The anode and cathode streams were arranged in a co-flow orientation from the upper left corner to the lower right corner of the fuel cell. After adjusting the fuel cell operating conditions, a period of 30 min was waited before acquiring radiographs. After the completion of radiography measurements at these three current densities, the fuel cell was also run at 1.2 A/cm^2 and 1.3 A/cm^2 without the radiography apparatus in place. From this part of the fuel cell polarization curve, shown at the top of Fig. 10, it is apparent that the development of significant mass transport resistance (often referred to as "flooding", where water accumulation within the fuel cell restricts transport of reactant molecules to the catalyst sites on the membrane electrode assembly) occurred beyond the range of current densities for which neutron radiographs were acquired.

Several important observations can be made from the data presented in Fig. 10. The overall quantity of water retained in the flow field channels was reduced as reactant flow and current density were increased. At 0.1 A/cm^2, red regions (corresponding to an $N\sigma T$ value of 0.05) are visible throughout the lower two-thirds of the test section, concentrated mainly in the 180° bends of the channels. As the load was increased to 0.5 A/cm^2 and then 1.0 A/cm^2, fewer of the red regions are visible, and a larger gradient in water concentration developed across the active area of the fuel cell. The images in Fig. 10 are visual representations of the matrix of $N\sigma T$ values. By summing the matrix elements in each image, a quantitative indication of the relative amounts of water can be obtained. For 0.1 A/cm^2, 0.5 A/cm^2, and 1.0 A/cm^2, the calculated sums of $N\sigma T$ are 9476, 8652, and 5470, respectively. Although the water produced in the cathodic oxygen reduction reaction increases proportionally with load, the volumetric flow rates of both hydrogen and air do as well for operation with constant stoichiometric ratios. It appears that for fully saturated reactant streams at 270 kPa, the higher channel gas velocity is sufficient to overcome the greater water production rate, resulting in less accumulated water within the flow field channels as the current density increases. However, despite the apparent change in water content as the operating conditions are varied, in all cases water tended to accumulate in the 180° bends of the flow field channels. This occurs as a result of the decreasing channel-to-channel pressure gradient as the flow approached the bends. In these regions, there is little driving force for liquid water transport either through the diffusion media or along the channel itself.

An unexpected observation from the images in Fig. 10 was that the water accumulation became concentrated in the central region of the fuel cell as the load was increased. Because the overall water content increases and reactant flow decreases along the flow field channels, it was expected that the water accumulation would be greatest near the cathode outlet, at the lower right hand corner of the radiographs. A water mass balance, computed by assuming that all product water stays on the cathode side and considering the pressure drop through the cell, indicated that the local water content increases monotonically from inlet to outlet. However, two features of the fuel cell hardware may have contributed to the observed trend. First, a ribbon heater wrapped around the periphery of the cell maintained the fuel cell temperature. Hence, the center of the cell was farthest from the heating source, and therefore had the highest rate of local heat loss. Because of the saturated conditions, a lower temperature in this region may have resulted in local condensation. The second factor is that the compressive force is known to be lowest at the center of the active area, despite the rather thick backing plates. This effect could result in increased flow through the diffusion media between channels, thereby locally reducing the gas velocity in the channels.

A second objective of the present experimental study was to assess the effect of cathode stoichiometric ratio on channel water retention at a relatively high load (1.0 A/cm^2). Because the average oxygen partial pressure increases near the catalyst sites with increasing air flow rate, it is expected that performance will improve. However, it is also of interest to determine if there is an additional benefit of

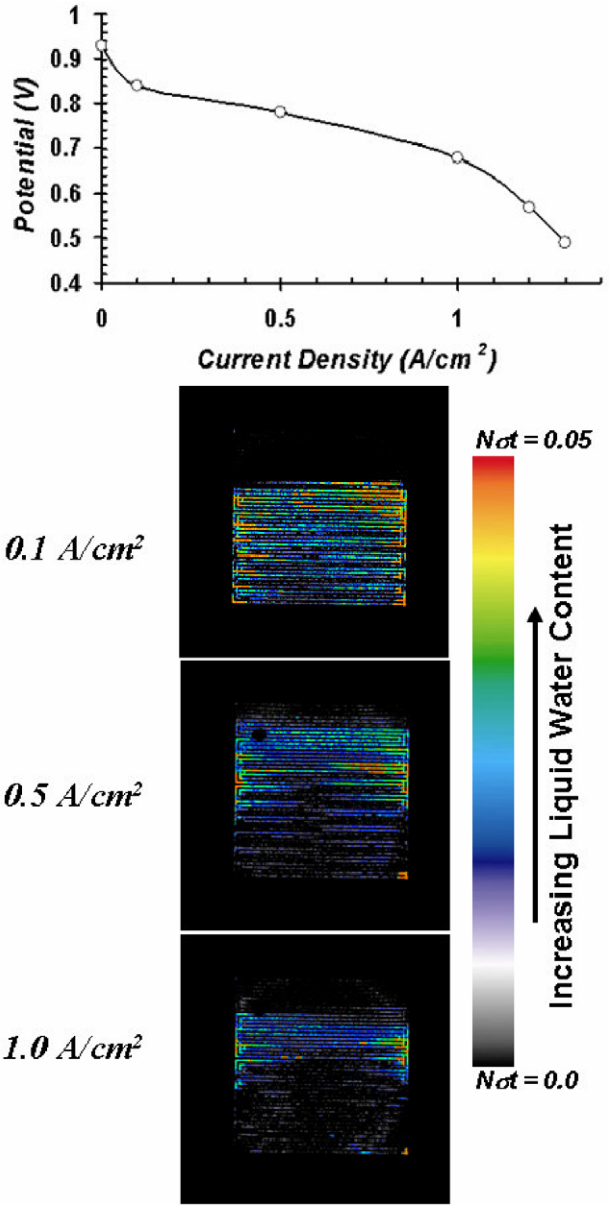

Fig. 10. Fuel cell polarization curve and averaged channel water images at three current densities (80 °C, 270 kPa, 100% inlet relative humidity, anode/cathode stoich = 2/1.3).

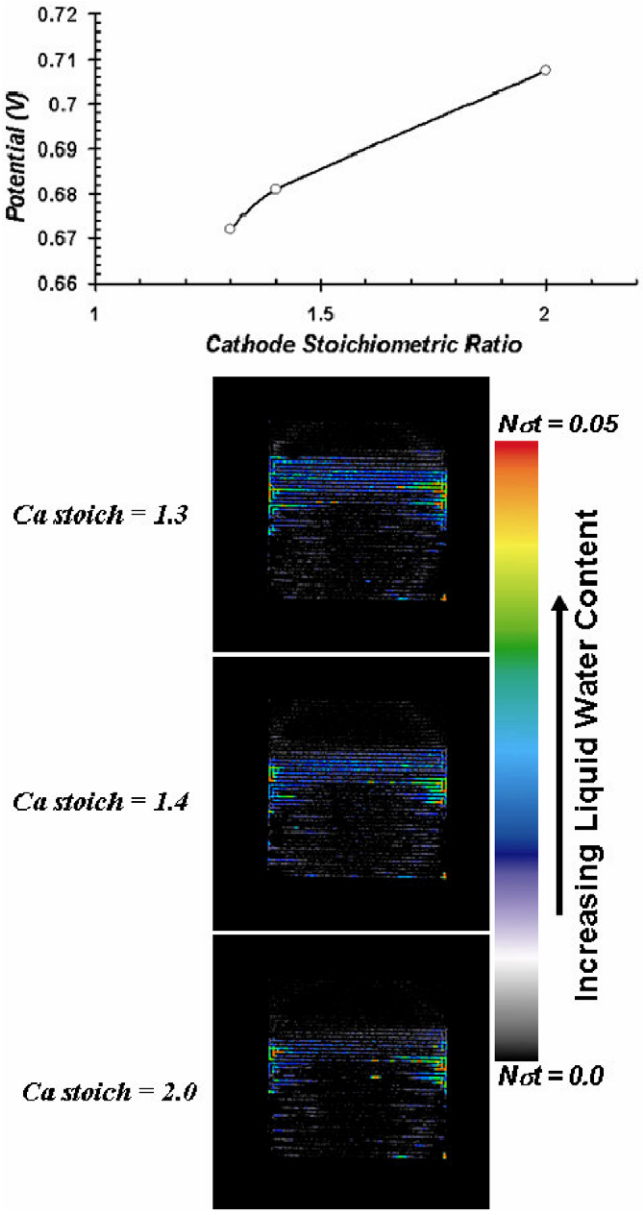

Fig. 11. Effect of cathode stoichiometric ratio on fuel cell voltage and associated averaged water images (1.0 A/cm^2, 80 °C, 270 kPa, 100% inlet relative humidity, anode stoich = 2.0).

increased reactant flow to clear accumulated water that can reduce the resistance of oxygen flow to catalyst sites at the cathode electrode. In Fig. 11, the flow channel water distributions are shown for the case of 1.0 A/cm^2 with cathode stoichiometric ratios of 1.3, 1.4, and 2.0. For the specific operating conditions with fully saturated inlet streams at 270 kPa, it is observed that there is a small effect on the amount of water accumulated within the fuel cell at different air flow rates, relative to the change observed in Fig. 10, even though there is a gain in cell voltage of about 35 mV. For these three conditions, the values of $N\sigma T$ are 5470, 4935, and 3628, respectively. If there is a beneficial effect of water removal, it must be due primarily to effects in the gas diffusion layer under the flow field lands, areas that are not interrogated in Figs. 10 and 11, due to the channel masking operation described in Fig. 9. The other possible explanation is that the observed channel water accumulation is actually on the anode side. Although the overall mass balance (including production, electro-osmotic drag, and back diffusion) would indicate that much more water should be present on the cathode side, it is difficult to conclusively separate anode and cathode water transport because the channels overlap over most of the active area, and the neutron radiograph provides a two-dimensional water distribution that is an average through the various components of the fuel cell (anode and cathode flow fields and diffusion media, and MEA). It was observed that water

was occasionally introduced into the fuel cell by condensation in the inlet reactant lines and could become trapped in the flow channels, especially at low load. This water would be less likely to be purged from the anode channels because of the roughly 2.5 times lower volumetric flow rate than the cathode channels for the same stoichiometric ratio.

4. Conclusions and future work

The present study has demonstrated that the neutron radiography technique is well suited for measurement of liquid water accumulation within an operating PEM fuel cell. Because the neutron cross-section for water is typically larger than the cross-sections for materials commonly used in fuel cell construction, this method is sensitive to small variations in local water content. The combined gradients in water concentration along the channels of the anode and cathode flow fields were clearly resolved. Moreover, it was observed that for the case of fully saturated reactant streams at 270 kPa, the amount of liquid water retained within the fuel cell decreases with increasing load, indicating that a higher gas velocity is sufficient to overcome the increased water production and maintain clear flow channels when operating at a current density of 1.0 A/cm^2. It was also determined that at this load, the cathode stoichiometric ratio has a relatively small influence on the amount of water accumulated. This observation suggests that increasing mass transport voltage loss at higher loads is the result of water accumulation in the soft goods of the cell (i.e., diffusion media, membrane-electrode assembly) as opposed to a channel water transport mechanism.

For future testing, several modifications can be made to improve the neutron radiography methods described herein and make it possible to extract additional quantitative data on the liquid water content:

- Modify the 50 cm^2 test cell hardware to improve neutron transmission. It is important to use thinner flow field plates that are constructed of less attenuating materials.
- Measure the neutron beam attenuation versus water thickness in order to accurately determine the macroscopic neutron cross-section ($\Sigma = N\sigma$) for partially bound water molecules. An approach using a water-filled wedge has been documented previously by Brenizer et al. [9]. Once this quantity is known, local distributions of the water thickness can be computed from the images shown in Figs. 8, 10, and 11.
- Because a significant length of time can elapse between acquisition of the baseline "dry" image and the operating cell images (the ratio of which is used to compute $N\sigma T$ via Eq. (5)), it is important to normalize the images for fluctuations in neutron beam intensity. It is possible that some extraneous image artifacts, such as the wire and hole seen on the left and right hand sides of the image in Fig. 8, are the result of variations in the neutron beam intensity over time.

As discussed in the Part 2 paper [10], some of these improvements have been implemented to enable extraction of accurate water mass data that can be correlated to fuel cell performance and the output from other system measurements, such as differential pressure.

Acknowledgments

This work was supported by the US Department of Commerce, the NIST Ionizing Radiation Division, the Director's office of NIST, the NIST Center for Neutron Research, and the Department of Energy interagency agreement No. DE-AI01-01EE50660.

References

[1] S.J.C. Cleghorn, C.R. Derouin, M.S. Wilson, S. Gottesfeld, A printed circuit board approach to measuring current distribution in a fuel cell, J. Appl. Electrochem. 28 (1998) 663–672.
[2] M.M. Mench, C.Y. Wang, M. Ishikawa, In situ current distribution measurements in polymer electrolyte fuel cells, J. Electrochem. Soc. 150 (2003) A1052–A1059.
[3] K. Tuber, D. Pocza, C. Hebling, Visualization of water buildup in the cathode of a transparent PEM fuel cell, J. Power Sources 124 (2003) 403–414.
[4] R.J. Bellows, M.Y. Lin, M. Arif, A.K. Thompson, D. Jacobson, Neutron imaging for in situ measurement of water transport gradients within Nafion in polymer electrolyte fuel cells, J. Electrochem. Soc. 146 (1999) 1099–1103.
[5] A.B. Geiger, A. Tsukada, E. Lehmann, P. Vontobel, A. Wokaun, G.G. Scherer, In situ investigation of two-phase flow in flow fields of PEFC's using neutron radiography, Fuel Cells 2 (2002) 92–98.
[6] R. Satija, D.L. Jacobson, M. Arif, S.A. Werner, In-situ neutron imaging technique for evaluation of water management systems in operating PEM fuel cells, J. Power Sources 129 (2004) 238–245.
[7] N. Pekula, K. Heller, P.A. Chuang, A. Turhan, M.M. Mench, J.S. Brenizer, K. Unlu, Study of water distribution and transport in a polymer electrolyte fuel cell using neutron radiography, Nucl. Instrum. Meth. Phys. Res. A 21 (2005) 134.
[8] D. Kramer, J. Zhang, R. Shimoi, E. Lehmann, A. Wokaun, K. Shinohara, G.G. Scherer, In situ diagnostic of two-phase flow phenomena in polymer electrolyte cells by neutron imaging Part A. Experimental, data treatment, and quantification, Electrochem. Acta 50 (2005) 2603–2614.
[9] J.S. Brenizer, K.W. Tobin, J.M. Hylko, D.D. McRae, R.W. Jenkins Jr., Quantitative measurement of equivalent water density in a burning cigarette, Mater. Eval. 45 (1987) 1310–1314.
[10] J.P. Owejan, T.A. Trabold, D.L. Jacobson, D.R. Baker, D.S. Hussey, M. Arif, In situ investigation of water transport in an operating PEM fuel cell using neutron radiography: Part 2 – Transient water accumulation in an interdigitated cathode flow field, Int. J. Heat Mass Transfer, in press, doi:10.1016/j.ijheatmasstransfer.2006.07.004.